Effect of Cu by Co substitution on $Ca_3Co_4O_9$ thermoelectric ceramics

Sh. Rasekh[1], M. A. Torres[2], G. Constantinescu[1], M. A. Madre[1], J. C. Diez[1], A. Sotelo[1]

[1]ICMA (UZ-CSIC), Dpto. de Ciencia y Tecnología de Materiales y Fluidos, C/María de Luna 3, E-50018, Zaragoza (Spain)

[2]Universidad de Zaragoza, Dpto. de Ingeniería de Diseño y Fabricación, C/María de Luna 3, E-50018, Zaragoza (Spain)

Abstract

$Ca_3Co_{4-x}Cu_xO_9$ polycristalline thermoelectric ceramics with small amounts of Cu have been synthesized by the classical solid state method. XRD data have shown that all the Cu has been incorporated into the $Ca_3Co_4O_9$ structure and no Cu-containing secondary phases have been produced. Apparent density measurements have shown that all samples are very similar, with densities around 75 % of the theoretical one. Electrical resistivity decreases when Cu content increases until x = 0.03 while Seebeck coefficient remains practically constant for all samples. The improvement in resistivity leads to higher power factor values than the obtained for the undoped samples.

Keywords: Sintering; Doping; Electrical properties; Thermopower.

Corresponding author: A. Sotelo

e-mail: asotelo@unizar.es

Address: Dept. Ciencia de Materiales; C/Mª de Luna, 3; 50018-Zaragoza; Spain

Tel: +34 976762617

Fax: +34 976761957

1. Introduction

Thermoelectric (TE) materials can transform a temperature difference to electrical power directly due to the well-known Seebeck effect. The conversion efficiency of such materials is quantified by the dimensionless figure of merit ZT, $TS^2/\rho\kappa$ (in which S^2/ρ is also called power factor, PF), where S is the Seebeck coefficient (or thermopower), ρ the electrical resistivity, κ the thermal conductivity, and T is the absolute temperature [1]. This important characteristic has focused attention on this type of materials in order to be applied as waste heat recovery devices [2] or solar thermoelectric generators [3]. Furthermore, they can also be used as heating/refrigeration devices [4].

Nowadays TE devices based on intermetallic materials, such as Bi_2Te_3 or $CoSb_3$, with high ZT values at relatively low temperatures, are industrially used, e.g. in vehicles exhaust. However, due to their degradation at high temperatures under air, they cannot be applied in devices working in these conditions. These limitations were overwhelmed by the discovery in 1997 of attractive thermoelectric properties in $Na_2Co_2O_4$ ceramics [5]. From the discovery of this thermoelectric oxide, much work has been performed on the cobaltite ceramics as promising thermoelectric materials for high temperature applications. The intense research work devoted on those ceramics led to the discovery and optimization of new compositions, such as $Ca_3Co_4O_9$, $LaCoO_3$, $Bi_2Sr_2Co_2O_9$ and $Bi_2Ca_2Co_2O_y$ with interesting thermoelectric properties and high working temperatures [6-9].

Crystallographic studies performed on those Co-based materials have demonstrated that they posses a monoclinic structure which is, in turn, composed of two different layers. These layers show an alternate stacking of a

common conductive CdI_2-type hexagonal CoO_2 layer with a two-dimensional triangular lattice and a block layer composed of insulating rock-salt-type (RS) layers. The two sublattices (RS block and CdI_2-type CoO_2 layer) possess common a- and c-axis lattice parameters and β angles, but different b-axis length, causing a misfit along the b-direction [10]. The high structural anisotropy of these materials leads to the formation of plate-like grains during the crystallisation process. This shape anisotropy opens the route to align preferentially the grains using physical, mechanical and/or chemical processes. Such processes should allow the alignment of the conducting planes leading to macroscopic properties comparable to those obtained on single crystals. Numerous methods have been reported to be efficient to produce well aligned bulk materials, in these or in similar anisotropic systems, such as hot uniaxial pressing [11], templated grain growth (TGG) [12], spark plasma sintering [13], microwave texturing [14], laser floating zone melting (LFZ) [15], electrically assisted laser floating zone [16], *etc*. The main drawbacks of these methods are due to different factors, as the relatively long treatments required for the two first ones, the high costs associated to the spark plasma and the strong dependence of the growth speed [14,17-20].

On the other hand, it has also been reported that the Seebeck coefficient values are governed by the incommensurability ratio and/or the charge of the RS block layer between the CoO_2 ones [21]. This characteristic provides the basis for the modification of thermoelectric properties of a given material via chemical substitutions. The most common ones substitute an alcaline-earth by a rare-earth, as Yb or Sb for Ca in $Ca_3Co_4O_9$ [22,23], or Yb for Sr in $La_{0.1}Sr_{0.9}TiO_3$ [24].

Other usual substitutions are Pb for Bi in $Bi_2Sr_2Co_{1.8}O_x$ or $Bi_2Ca_2Co_{1.7}O_x$ [25,26], or metallic Ag additions in $Ca_3Co_4O_9$ or $Bi_2Sr_2Co_{1.8}O_x$ [27,28].

The aim of this work is to study the effect of Cu for Co substitution, in small amounts, on the microstructural and thermoelectric characteristics of sintered $Ca_3Co_{4-x}Cu_xO_y$ bulk materials prepared by the classical solid state synthetic route.

2. Experimental

$Ca_3Co_{4-x}Cu_xO_9$ polycristalline ceramic materials, with x = 0.00, 0.01, 0.03, and 0.05, were prepared by the conventional solid state route using commercial $CaCO_3$ (Panreac, 98 + %), Co_2O_3 (Aldrich, 98 + %), and CuO (Panreac, 98 + %) powders as starting materials. They were weighed in the appropriate proportions, well mixed and ball milled for 30 minutes at 300 rpm, in acetone media, in an agate ball mill. The obtained slurry has been heated under an infrared drying system until all the acetone has been evaporated. The dry mixture was then manually milled in order to avoid the presence of agglomerates in the next steps. After milling, the homogeneous mixture was thermally treated twice at 750 and 800ºC for 12h under air, with an intermediate manual milling in order to assure the total decomposition of alcaline-earth carbonates, as reported previously [29]. After thermal treatment, the powders were uniaxially pressed at 400 MPa for 1 minute in order to obtain green ceramic parallelepipeds (~ 3 mm x 3 mm x 14 mm), with an adequate size for their thermoelectric characterization. These materials were subsequently sintered in the optimal conditions for this system, consisting in one step heating at 910 ºC for 24 h with a final furnace cooling.

Powder X-ray diffraction (XRD) patterns have been systematically recorded in order to identify the different phases in the thermoelectric sintered materials. Data have been collected at room temperature, with 2θ ranging between 5 and 60 degrees, using a Rigaku D/max-B X-ray powder diffractometer working with Cu Kα radiation. Apparent density measurements have been performed on several samples for each composition after sintering, using 4.677 g/cm^3 as theoretical density [30].

Microstructural observations were performed on longitudinal polished sections of the samples, using a JEOL 6000 scanning electron microscope fitted with an energy dispersive spectrometry (EDS) analyzer. Micrographs of polished sections of the samples have been used to analyze the different phases and their distribution. Fractured transversal sections of the samples were observed with a Field Emission Scanning Electron Microscope (FESEM, Carl Zeiss Merlin), to observe grain morphology and sizes distribution. Electrical resistivity and Seebeck coefficient were simultaneously determined by the standard dc four-probe technique in a LSR-3 measurement system (Linseis GmbH), in the steady state mode and at temperatures ranging from 50 to 800 ºC under He atmosphere. With the electrical resistivity and thermopower data, the power factor has been calculated in order to determine the samples performances. These properties have been compared with the results obtained in the undoped samples and with those reported in the literature at low temperature (~ 50 ºC), where oxygen diffusion is negligible, to avoid the influence of the atmosphere on the compared values.

3. Results and discussion

Powder XRD patterns for the different $Ca_3Co_{4-x}Cu_xO_9$ samples are displayed in Fig. 1 (from 5 to 40º for clarity). From these data, it is clear that all the samples have very similar diffraction patterns. As can be seen in Fig. 1a, corresponding to the undoped samples, the highest peaks have been associated to the thermoelectric $Ca_3Co_4O_9$ phase, indicated by the reflection planes, and in agreement with previously reported data [31] and the peak at about 31º, identified by *, corresponds to the $Ca_3Co_2O_6$ phase [31]. On the other hand, the peak at around 28.65 degrees (indicated by • in Fig. 1d) corresponds to the (111) diffraction plane of Si used as reference. When Cu is added to the samples, some new peaks, belonging to the $Ca_3Co_2O_6$ phase [31], appear (identified by * in Fig 1d), indicating a slight increase on this phase content when the amount of Cu is raised. All these observations indicate that samples are composed by $Ca_3Co_4O_9$ as the major phase, accompanied by small amounts of $Ca_3Co_2O_6$. This is a clear indication that all added Cu has been incorporated into the $Ca_3Co_4O_9$ structure as no other Cu-containing phases are detected. Moreover, no shift on the $Ca_3Co_4O_9$ peaks has been detected due to the small amount of Cu and the very small difference in size between Co and Cu.

General SEM observations performed on polished sections have shown that porosity seems to decrease when Cu content is increased, as illustrated in Fig. 2 where representative views of all the samples are displayed. This behaviour can be explained when considering the Ca-Co-O [32], and Ca-Cu-O [33] phase equilibrium diagrams. In these diagrams, the eutectic point is at about 1350 ºC for the CaO-CoO system which is far higher than the sintering temperature. On the other hand, the temperature for the CaO-CuO eutectic point is reduced to

around 1000 ºC, closer to the sintering conditions than the above mentioned. As a consequence, a slight improvement on the densification should be expected with the increase on the Cu contents.

In order to check the effect of Cu content on the porosity of the bulk sintered materials, apparent density measurements have been performed for all samples. At least three samples for each composition were measured for three times in order to minimize measurement errors. The obtained mean values, together with their standard error, are represented in Fig. 3. As it can be clearly seen in the figure, the density values slightly increase with increasing the Cu content. On the other hand, the errors also follow the same trends, indicating a higher dispersion on the obtained values. In any case, the density data confirm the SEM observations and their explanation in the above paragraph. When considering the relative density, compared with the theoretical one, the values are ranging from around 72 % for the pure samples, to about 75 % for the 0.05 Cu-substituted ones.

Fig. 4 shows a representative fractured surface performed on the pure $Ca_3Co_4O_9$ material. As it is illustrated in the micrograph, all the samples are composed of randomly oriented plate-like grains. Moreover, it can be observed that the grain sizes range from less than 1 μm to more than 5 μm in the ab plane. This broad grain size distribution is expected as it is one of the typical trademarks for the solid state synthetic methods. On the other hand, they possess much smaller sizes along the c-axis due to the preferential grain growth habit of this kind of materials, as can also be observed in the micrograph.

The temperature dependence of electrical resistivity, as a function of the Cu content, is shown in Fig. 5. The ρ (T) curves show a decrease of resistivity when Cu is added, compared with the undoped samples. All the curves show a semiconducting-like ($d\rho/dT \leq 0$) behaviour, from room temperature to around 450 ºC, in agreement with previously reported data in this system where the charge transport process is a hole hopping from Co^{4+} to Co^{3+} [34]. At higher temperatures, this behaviour changes to a metallic-like ($d\rho/dT \geq 0$) one where the charge carriers are transported in the valence or conduction band [35]. In these samples, room temperature resistivity values decrease when the Cu substitution is increased until 0.03. This effect can be explained by the lower oxidation state of Cu (+2) than the average one for Co (between +3 and +4), increasing the hole concentration, and decreasing resistivity [35]. Further Cu addition increases resistivity due to the raise on the $Ca_3Co_2O_6$ phase content. In any case, the lowest measured room temperature resistivity values (~ 19 mΩ.cm for the 0.03 Cu-substituted samples) is around the best values obtained for $Ca_3Co_4O_9$ samples produced by more sophisticated methods. As examples, it can be considered the values obtained in samples consolidated by spark plasma sintering (15-18 mΩ.cm) [36] or produced by solution methods (~ 16 mΩ.cm) [29].

Fig. 6 shows the variation of the Seebeck coefficient with the temperature, as a function of the Cu doping. In the plot, it can be clearly seen that the sign of the thermopower is positive for the entire measured temperature range, which confirms a conduction mechanism mainly governed by holes. The values of the Seebeck coefficient increase with the temperature, with similar values and behaviour for all the samples, indicating that Cu addition does not modify

significantly the relationship between Co^{+3} and Co^{+4} [37]. The obtained values at room temperature (~ 130 μV/K) are slightly higher than those reported elsewhere (~ 125 μV/K) at the same temperature [38]. On the other hand, the maximum Seebeck coefficient value (~ 200 μV/K) obtained at 800 ºC is significantly higher than the best values obtained for $Ca_3Co_4O_9$ samples consolidated by spark plasma sintering (170-175 μV/K) at about 625 ºC [36]. The similar values obtained for all samples indicate that small Cu addition does not affect, in a great extent, the $Ca_3Co_4O_9$ conduction band.

As it was indicated previously about the charge-transport process by hopping in these compounds, the temperature dependence of the electrical conductivity can be described as:

$$\sigma.T \propto \exp (E/k_B.T)$$

where E, k_B, and T are the activation energy, Boltzmann constant, and absolute temperature, respectively. The activation energy values are obtained from the log (σT) *versus* 1/T plot as the curve fit slope in the different samples below T*, as illustrated in Fig. 7. T* is defined as the temperature where the behaviour of the samples changes from semiconducting to metallic one. The calculated values have been found to be around 40 meV in all cases, confirming that Cu addition does not modify appreciably the $Ca_3Co_4O_9$ conduction band.

In order to evaluate the thermoelectric performances of these materials, the power factor has been calculated. The temperature dependence of the power factor, estimated from the data represented in Figs. 5 and 6 is plotted in Fig. 8. When considering PF values at around 50 ºC (~ room temperature), it can be clearly seen that the 0.01, and 0.03 Cu-doped samples possess slightly higher PF values than the undoped ones. The maximum increase is obtained for the

0.03 Cu-doped samples (~ 10 % higher than the undoped ones). On the other hand, the 0.05 Cu-doped samples show the lowest PF values due to the higher $Ca_3Co_2O_6$ phase content. The highest PF value obtained at 800 ºC (around 0.21 mW/K^2.m) for the 0.03 Cu-doped samples is about 10 % higher than the obtained for the undoped samples.

4. Conclusions

This paper demonstrates that $Ca_3Co_{4-x}Cu_xO_9$ nominal composition samples improve thermoelectric properties without modifying the crystal structure for small Cu amounts ($x \leq 0.03$). Further Cu addition diminishes thermoelectric performances due to the formation of $Ca_3Co_2O_6$ secondary phase. The optimal Cu for Co substitution has been determined using the values of the power factor at 50 and 800 ºC, which is maximum for the 0.03 Cu-doped samples with values around 0.10 and 0.21 mW/K^2.m, respectively, which are about 10 % higher than the obtained for the undoped samples.

Acknowledgements

The authors wish to thank the Gobierno de Aragón (Research Groups T12 and T87) for financial support. The technical contributions of C. Estepa, and C. Gallego are also acknowledged. Sh. Rasekh acknowledges a JAE-PreDoc 2010 grant from CSIC.

References

1. D. M. Rowe, in Thermoelectrics handbook: macro to nano, ed By D. M. Rowe (CRC Press, Boca Raton, FL, 2006) p. 1-3

2. G. Mahan, B. Sales, J. Sharp, Phys. Today 50, 42 (1997)

3. H. Naito, Y. Kohsaka, D. Cooke, H. Arashi, Solar Energy 58, 191 (1996)

4. C. M. Kim, Y. J. Hwang, Y. H. Ryu, US Patent US6393842. May, 2002.

5. I. Terasaki, Y. Sasago, K. Uchinokura, Phys. Rev. B 56, 12685 (1997)

6. Y. Huang, B. Zhao, J. Fang, R. Ang, Y. Sun, J. Appl. Phys. 110, 123713 (2011)

7. F. Li, J. F. Li, J. H. Li, F. Z. Yao, Phys. Chem. Chem. Phys. 14, 12213 (2012)

8. J. J. Shen, X. X. Liu, T. J. Zhu, X. B. Zhao, J. Mater. Sci. 44, 1889 (2009)

9. X. G. Luo, Y. C. Jing, H. Chen, X. H. Chen, J. Crystal Growth 308, 309 (2007)

10. Y. Miyazaki, Solid State Ionics 172, 463 (2004)

11. V. Garnier, R. Caillard, A. Sotelo, G. Desgardin, Physica C 319, 197 (1999)

12. H. Itahara, C. Xia, J. Sugiyama, T. Tani, J. Mater. Chem. 14, 61 (2004)

13. J. G. Noudem, D. Kenfaui, D. Chateigner, M. Gomina, J. Electronic. Mater. 40, 1100 (2011)

14. S. Marinel, D. Bourgault, O. Belmont, A. Sotelo, G. Desgardin, Physica C 315, 205 (1999)

15. A. Sotelo, E. Guilmeau, M. A. Madre, S. Marinel, J. C. Diez, M. Prevel, J. Eur. Ceram. Soc. 27, 3697 (2007)

16. N. M. Ferreira, Sh. Rasekh, F. M. Costa, M. A. Madre, A. Sotelo, J.C. Diez, M. A. Torres, Mater. Lett. 83, 144 (2012)

17. A. Sotelo, E. Guilmeau, M. A. Madre, S. Marinel, S. Lemmonier, J. C. Diez, Bol. Soc. Esp. Ceram. V. 47, 225 (2008)

18. J. C. Diez, E. Guilmeau, M. A. Madre, S. Marinel, S. Lemmonier, A. Sotelo, Solid State Ionics 180, 827 (2009)

19. Sh. Rasekh, G. Constantinescu, M. A. Torres, M. A. Madre, J. C. Diez, A. Sotelo, Adv. Appl. Ceram. 111, 490 (2012)

20. G. Constantinescu, Sh. Rasekh, M. A. Torres, M. A. Madre, J. C. Diez, A. Sotelo, Scripta Mater. 68, 75 (2013)

21. A. Maignan, D. Pelloquin, S. Hébert, Y. Klein, M. Hervieu, Bol. Soc. Esp. Ceram. V. 45, 122 (2006)

22. X. Y. Song, Y. Chen, S. Chen, E. Barbero, E. L. Thomas, P. Barnes, Solid State Commun. 152, 1509 (2012)

23. S. Demirel, M. A. Aksan, S. Altin, J. Mater. Sci.: Mater. Electron. 23, 2251 (2012)

24. H. Wang, C. Wang, Ceram. Int. 39, 941 (2013)

25. A. Sotelo, Sh. Rasekh, E. Guilmeau, M. A. Madre, M. A. Torres, S. Marinel, J. C. Diez, Mater. Res. Bull. 46, 2537 (2011)

26. A. Sotelo, E. Guilmeau, Sh. Rasekh, M. A. Madre, S. Marinel, J. C. Diez, J. Eur. Ceram. Soc. 30, 1815 (2010)

27. F. P. Zhang, X. Zhang, Q. M. Lu, J. X. Zhang, Y. Q. Liu, G. Z. Zhang, Solid State Ionics 201, 1 (2011)

28. A. Sotelo, M. A. Torres, G. Constantinescu, Sh. Rasekh, J. C. Diez, M. A. Madre, J. Eur. Ceram. Soc. 32, 3745 (2012)

29. A. Sotelo, G. Constantinescu, Sh. Rasekh, M. A. Torres, J. C. Diez, M. A. Madre, J. Eur. Ceram. Soc. 32, 2415 (2012)

30. Y. C. Liou, W. C. Tsai, W. Y. Lin, U. R. Lee, J. Aust. Ceram. Soc. 44, 17 (2008)

31. E. Woermann, A. Muan, J. Inorg. Nucl. Chem. 32, 1455 (1970)

32. D. Sedmidubský, V. Jakes, O. Jankovský, J. Leitner, Z. Sofer, J. Hejtmánek, J. Solid State Chem. 194, 199 (2012)

33. R. S. Roth, N. M. Hwang, C. J. Rawn, B. P. Burton, J. J. Ritter, J. Am. Ceram. Soc. 74, 2148 (1991)

34. Y. H. Lin, J. Lan, Z. J. Shen, Y. H. Liu, C. W. Nan, J. F. Li, Appl. Phys. Lett. 94, 072107 (2009)

35. S. Pinitsoontorn, N. Lerssongkram, N. Keawprak, V. Amornkitbamrung, J. Mater. Sci.: Mater. Electron. 23, 1050 (2012)

36. D. Kenfaui, G. Bonnefont, D. Chateigner, G. Fantozzi, M. Gomina, J. G. Noudem, Mater. Res. Bull. 45, 1240 (2010)

37. W. Koshibae, K. Tsuitsui, S. Maekawa, Phys. Rev. B 62, 6869 (2000)

38. Y. Wang, Y. Sui, X. Wang, W. Su, X. Liu, J. Appl. Phys. 107, 033708 (2010)

Figure captions:

Figure 1. Powder X-ray diffraction patterns obtained for the samples; x = 0.00 (a); 0.01 (b); 0.03 (c); and 0.05 (d). The difraction planes indicate the $Ca_3Co_4O_9$ phase and the * the $Ca_3Co_2O_6$ ones. The • symbol identifies the (111) diffraction peak of Si, used as reference.

Figure 2. General SEM micrographs performed on polished sections of $Ca_3Co_{4-x}Cu_xO_9$ samples; x = 0.00 (a); 0.01 (b); 0.03 (c); and 0.05 (d). Porosity can be distinguished from the grey ceramic matrix.

Figure 3. Apparent density values of $Ca_3Co_{4-x}Cu_xO_9$ samples, together with their standard errors, as a function of Cu-content.

Figure 4. SEM micrograph performed on a representative fractured section of the $Ca_3Co_4O_9$ sample formed by randomly oriented plate-like grains.

Figure 5. Temperature dependence of the electrical resistivity, as a function of Cu content in $Ca_3Co_{4-x}Cu_xO_9$ samples, for x = 0.00 (●); 0.01 (■); 0.03 (◆); and 0.05 (▲).

Figure 6. Temperature dependence of the Seebeck coefficient as a function of Cu content in $Ca_3Co_{4-x}Cu_xO_9$ samples, for x = 0.00 (●); 0.01 (■); 0.03 (◆); and 0.05 (▲).

Figure 7. Log (σT) *versus* 1000/T plot for all the samples. The slopes of the fittings are nearly the same in all cases, below T*. T* indicates the metallic-to-semiconducting transition temperature.

Figure 8. Temperature dependence of the power factor as a function of Cu content in $Ca_3Co_{4-x}Cu_xO_9$ samples, for x = 0.00 (●); 0.01 (■); 0.03 (◆); and 0.05 (▲).

Figure 1

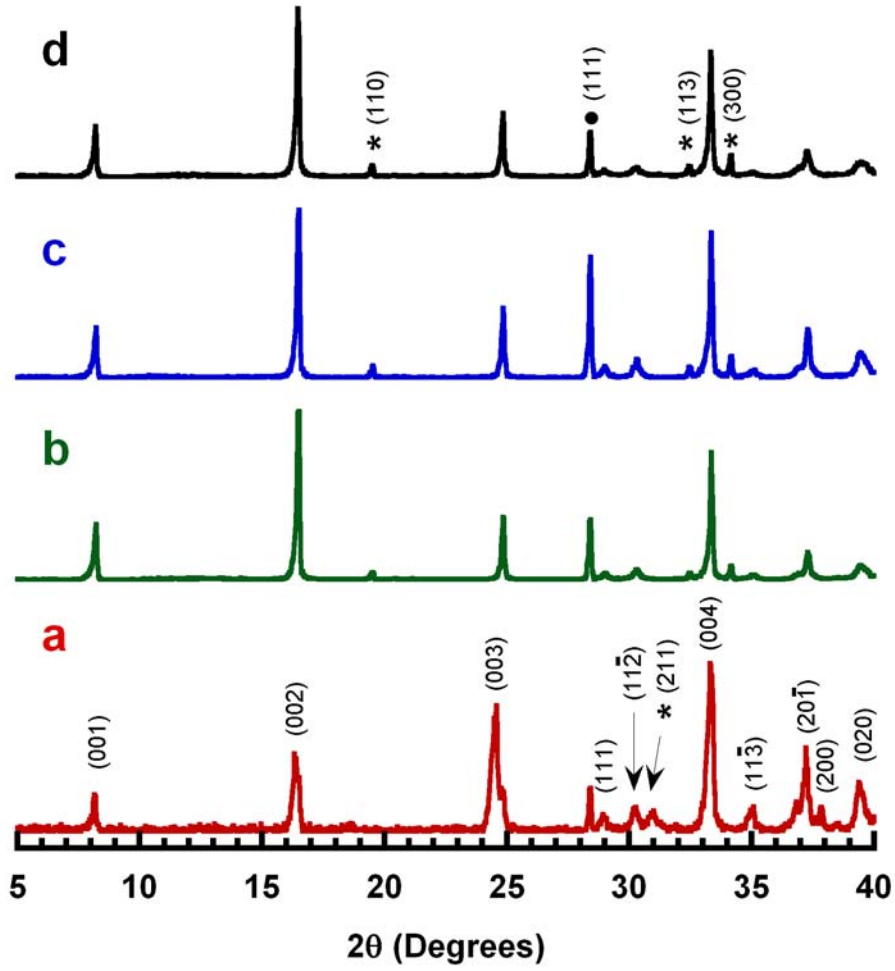
d
c
b
a
* (110)
(111)
* (113)
* (300)
(001)
(002)
(003)
(111)
(11$\bar{2}$)
* (211)
(004)
(11$\bar{3}$)
(20$\bar{1}$)
(200)
(020)
5
10
15
20
25
30
35
40
2θ (Degrees)

Figure 2

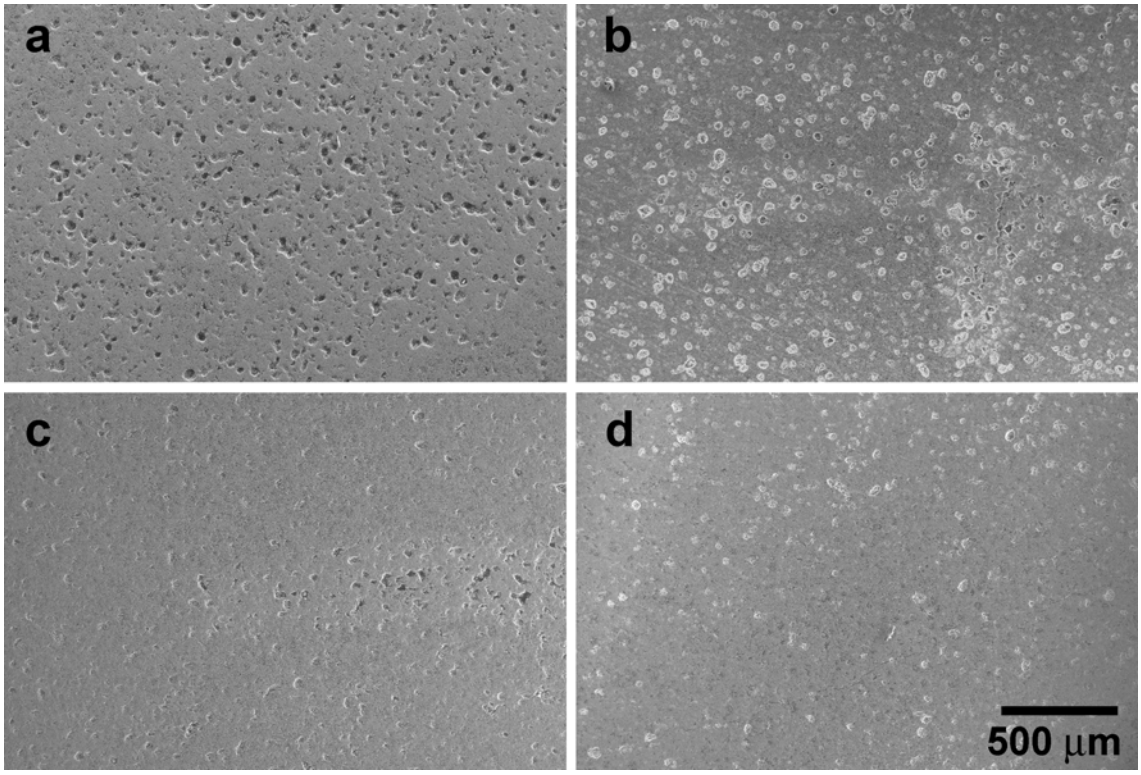

Figure 3

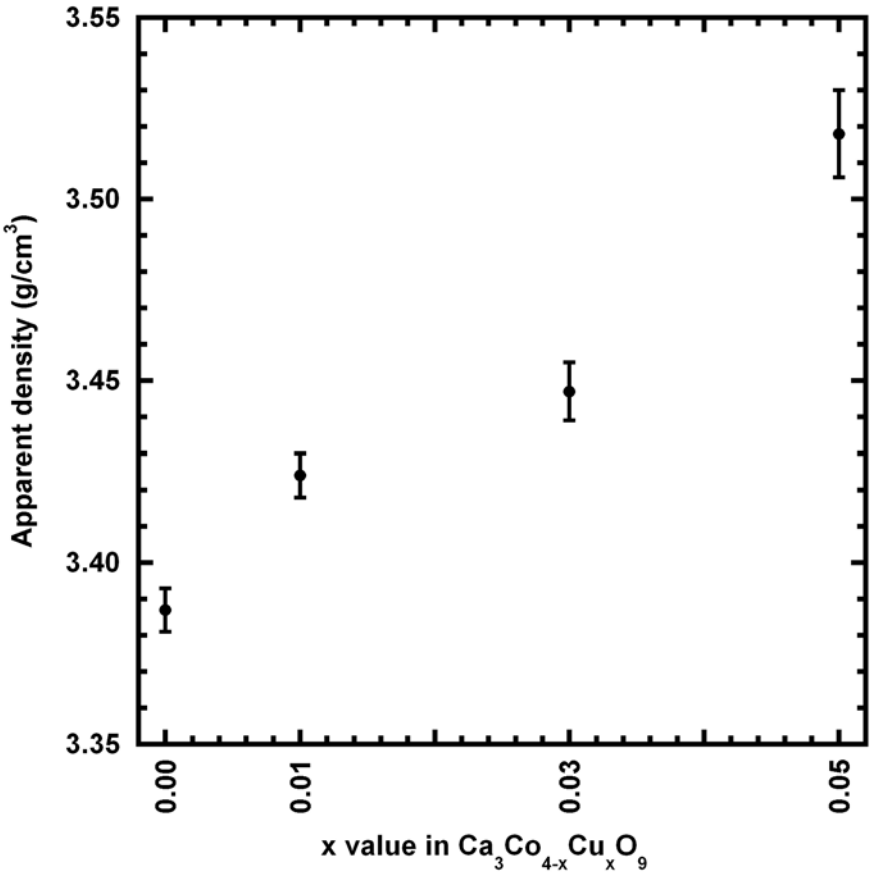
3.55
3.50
3.45
3.40
3.35
Apparent density (g/cm3)
0.00
0.01
0.03
0.05
x value in Ca3Co4-xCuxO9

Figure 4

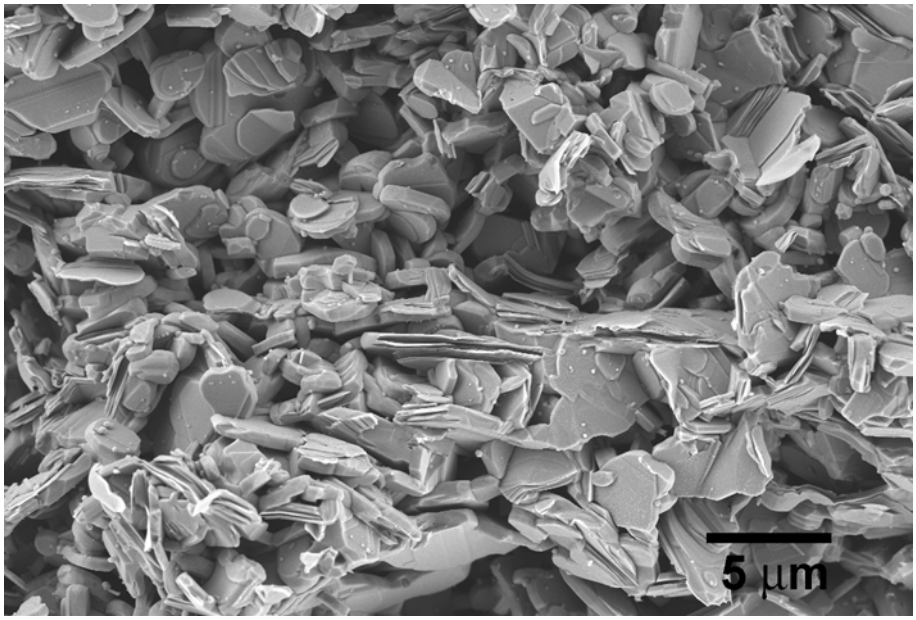

Figure 5

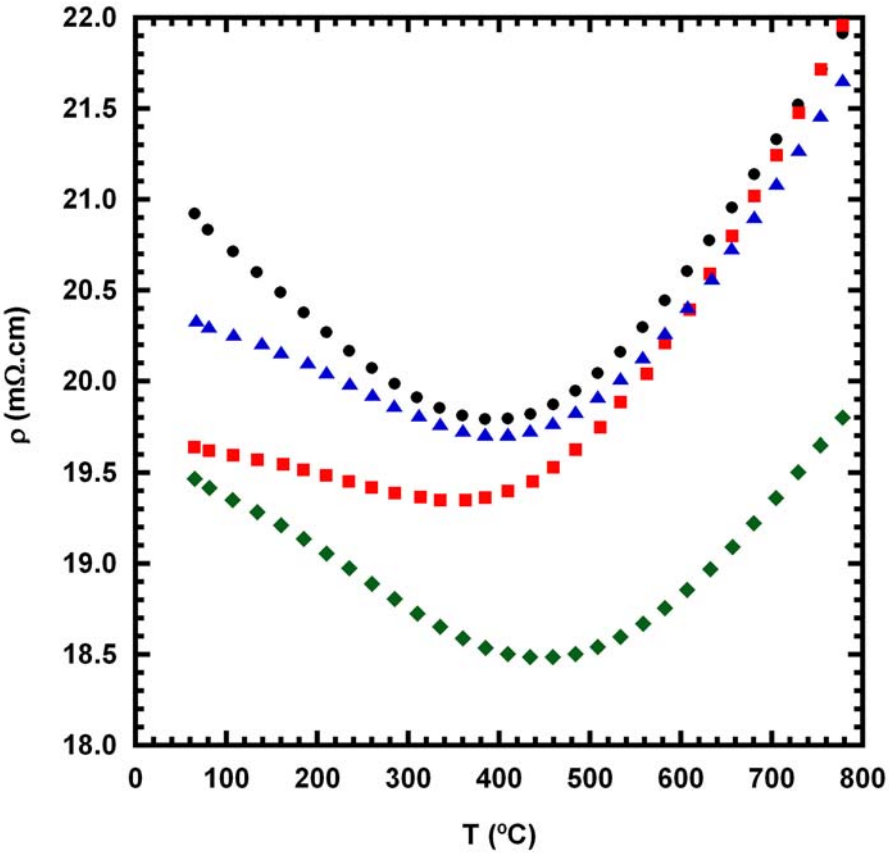
22.0
21.5
21.0
20.5
20.0
19.5
19.0
18.5
18.0
ρ (mΩ.cm)
0
100
200
300
400
500
600
700
800
T (°C)

Figure 6

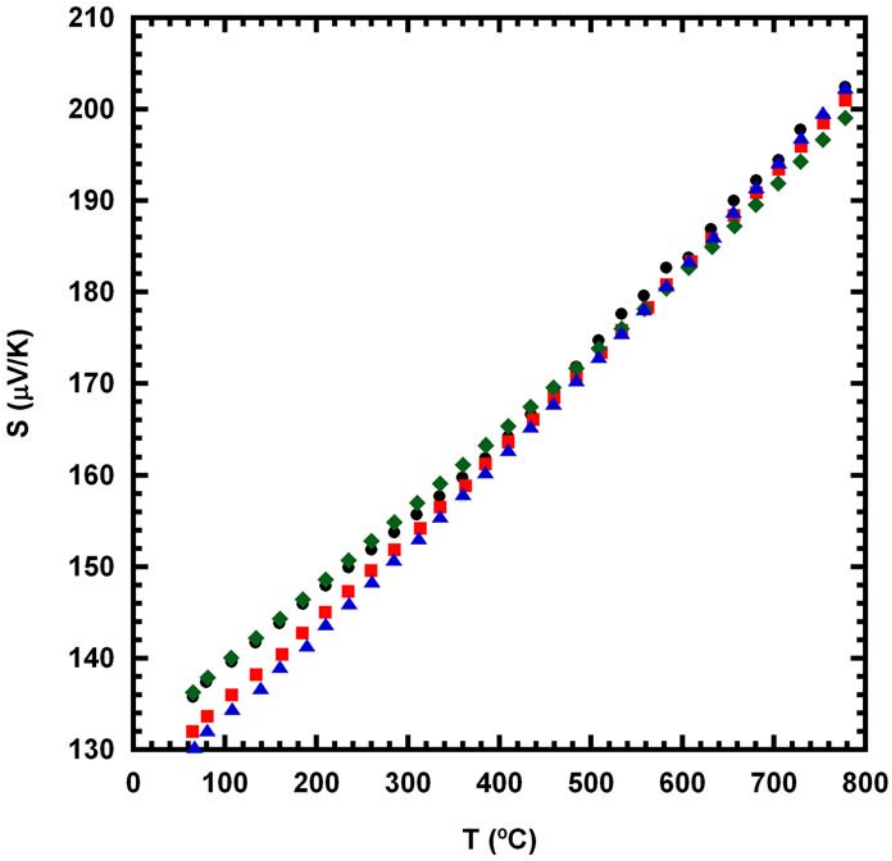
S (μV/K)
T (°C)
210
200
190
180
170
160
150
140
130
0
100
200
300
400
500
600
700
800

Figure 7

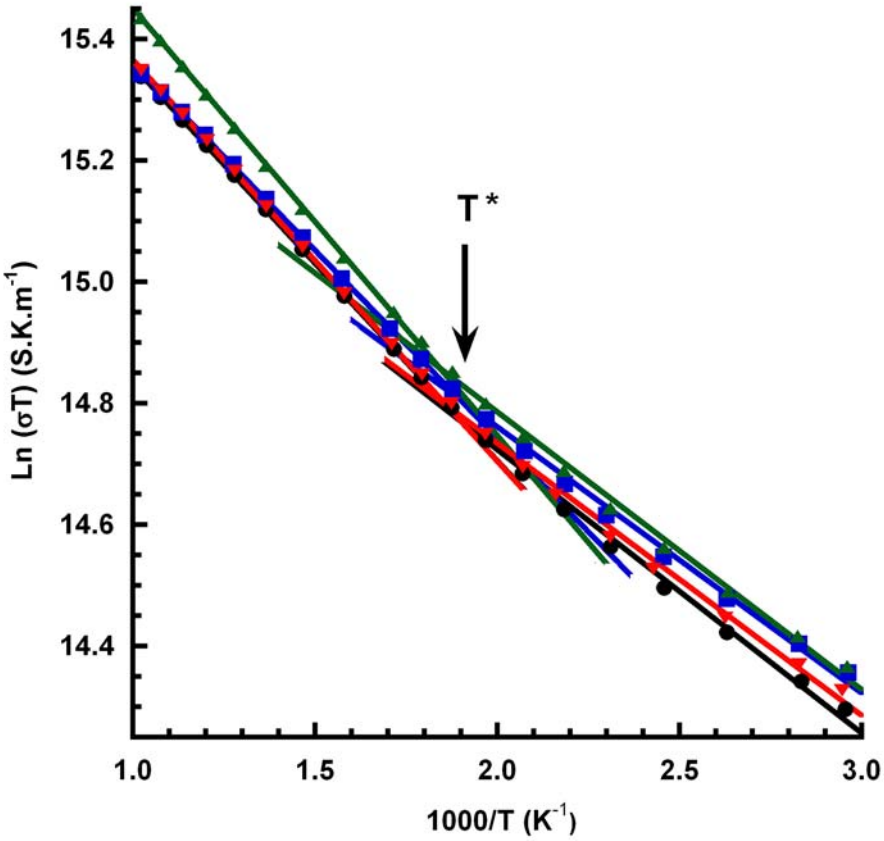

Figure 8

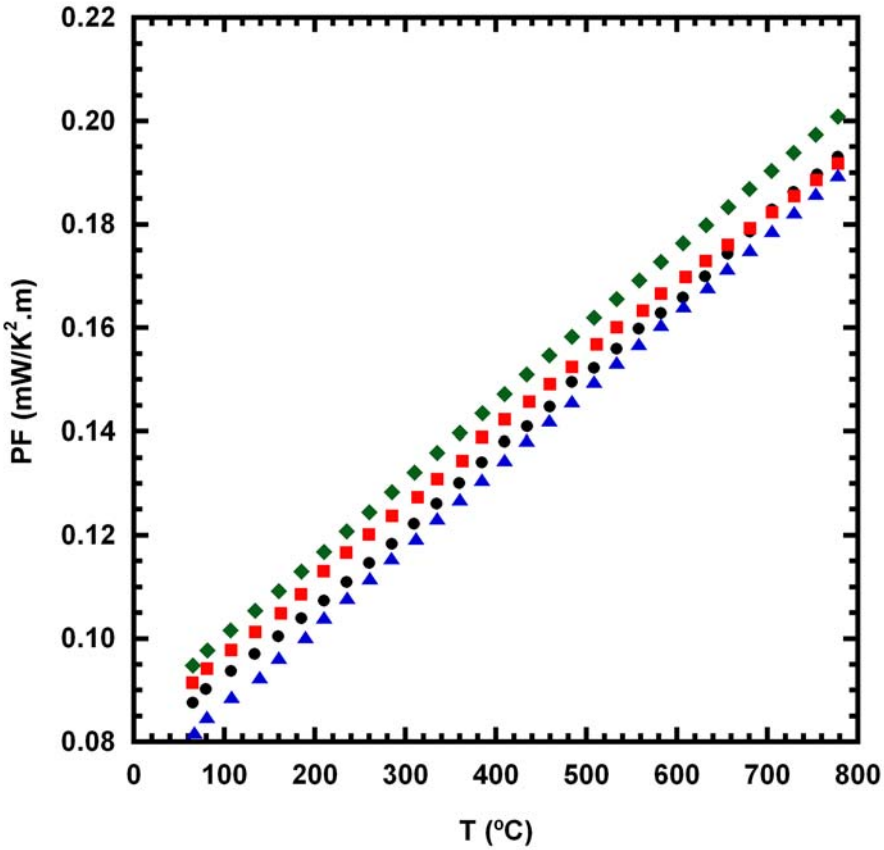
0.22
0.20
0.18
0.16
0.14
0.12
0.10
0.08
PF (mW/K^2.m)
0
100
200
300
400
500
600
700
800
T (°C)